

Banner appropriate to article type will appear here in typeset article

# Reynolds Number Effects on Lift Enhancement Mechanisms of Dragonfly Wings: Their Effective Ranges and Determination by Local Reynolds Numbers

Yusuke Fujita and Makoto Iima<sup>†</sup>

Graduate School of Integrated Sciences for Life, Hiroshima University, 1-7-1, Kagamiyama, Higashi-Hiroshima, Hiroshima, 739-8521, Japan

(Received xx; revised xx; accepted xx)

A corrugated structure, rather than a smooth surface, is a characteristic feature of insect wings (e.g., dragonfly wings), which enhances their aerodynamic performance at low Reynolds numbers ( $Re \approx O(10^3)$ ). However, the mechanisms responsible for these improvements remain largely unexplored. Previous studies have shown that a secondary vortex forms on a flat wing, opposite in sign to the leading-edge vortex (LEV). At  $Re = 4000$ , the lift enhancement in the corrugated wing is associated with vortex collapse and confinement within the V-shaped region, a part of corrugated structure. Conversely, when there was no lift improvement, the vortex remained intact and erupted without collapsing. In addition, the alternating vortices within the V-shaped region, comprising a negative vortex originating from the LEV and a positive vortex from the secondary vortex, induced a strong negative pressure, thereby further enhancing the lift. However, the working range of these mechanisms has yet to be investigated. In this study, lift enhancement was investigated over a broader Reynolds number range ( $100 \leq Re \leq 4000$ ), focusing on the effective ranges. No characteristic mechanism was observed for  $100 \leq Re \leq 500$ . For  $1000 \leq Re \leq 4000$ , the alternating vortices around the V-shaped region were correlated with the improved aerodynamic performance. Furthermore, for  $2000 \leq Re \leq 4000$ , the secondary vortex collapse plays a major role in lift enhancement. These findings demonstrate that the lift enhancement mechanisms for corrugated wings operate within distinct working ranges depending on the Reynolds number, thereby providing insights into bioinspired aerodynamic designs.

**Key words:**

## 1. Introduction

Flying animals and vehicles are of various sizes, ranging from microscopic insects, such as thrips, to aeroplanes. Accordingly, the Reynolds number ( $Re$ ) ranges from  $O(10^1)$ - $O(10^7)$  (Shyy *et al.* 2016; Eldredge & Jones 2019; Liu *et al.* 2024), where  $Re = \frac{cU_{ref}}{\nu}$ , where  $\nu$  is

<sup>†</sup> Email address for correspondence: iima@hiroshima-u.ac.jp

**Abstract must not spill onto p.2**

the kinematic viscosity,  $c$  is the wing-chord length, and  $U_{\text{free}}$  is the reference velocity, such as the average flight speed. The lift generation mechanism of an aeroplane at  $Re \geq O(10^6)$  can be explained by the steady wing theory based on the Kutta-Joukowski theorem (Landau & Lifshitz 2013). However, this theory cannot be applied to insect flights with flapping wings at  $Re = O(10^3)$  (Ellington 1984). Therefore, unsteady wing motion, such as flapping motion, is the key to understanding insect flight.

When insects perform a flapping motion, a leading-edge vortex (LEV) is generated in the upper part of the wing. LEV has also been observed in insects, bats, and hummingbirds (Chin & Lentink 2016). As the pressure at the vortex centre is low, the LEV contributes to the enhancement of lift. Therefore, LEV dynamics are important for flapping flights at low Reynolds numbers (Shyy *et al.* 2016; Ellington *et al.* 1996; Sane 2003; Liu *et al.* 2024).

In addition to wing motion and the Reynolds number, wing structure differs significantly between insects and airplanes. The cross-sectional geometry of the wings of many insects such as dragonflies, bees, and cicadas can be described as a combination of V-shaped structures and other geometric shapes categorized as corrugated wings (Dudley 2002). The structure of corrugated wings is widely regarded as providing mechanical assistance in the flapping motion (Bomphrey *et al.* 2016; Newman & Wootton 1986; Rajabi *et al.* 2016) and sensing processes associated with foraging, escape, and travel (Bomphrey *et al.* 2016; Uhrhan *et al.* 2024). In addition, it has been postulated that this structure has advantages in terms of lift generation. Corrugated wings have the potential to exhibit high wing performance in the low-Reynolds-number region ( $Re \approx O(10^3)$ ) and are expected to be applied in the design of small flying robot wings (Obata *et al.* 2014).

Most previous studies that assessed the aerodynamic performance of corrugated wings were designed to evaluate their functionality under specific gliding conditions: the mean flows of low angle of attack (AoA) conditions. Obata & Sinohara (2009) showed the superior flight stability of a corrugated wing at an AoA of  $5^\circ$  in  $Re \approx 7000$ . Kesel (2000) evaluated the aerodynamic performance of a corrugated wing model based on measurements from a real-life dragonfly wing, flat wing model, and filled wing model of a corrugated wing. They conducted wind-tunnel experiments at  $Re \geq 10\,000$ . The results indicated that the corrugated wing generated significantly higher lift coefficients owing to the steady negative pressure region formed in the valleys on both the upper and lower surfaces. Bomphrey *et al.* (2016) reported an improved lift-to-drag ratio at low AoA at  $Re = 730$ . More recently, Narita & Chiba (2024) scanned the three-dimensional data of the hind wings of a real-life dragonfly (*Pantala Flavescens*), performed a numerical analysis of the flow at  $Re = 4077$ , and reported that corrugation may contribute to improved wing performance under gliding conditions (with a low AoA). In addition, Bauerheim & Chapin (2020) suggested that the unsteady flow created by the corrugated wing structure is important, even under gliding conditions (with a low AoA) at  $Re = 6000$ .

As described above, most conventional studies evaluating the performance of corrugated wings have focused on static characteristics that implicitly assume gliding flight. These characteristics cannot be applied to flapping flights, which are the typical flight strategies of insects (Rees 1975; Meng & Sun 2011, 2013; Zhang *et al.* 2015; Ansari *et al.* 2019). Therefore, the authors aimed to clarify the relationship between the structure of the corrugated wing and the lift generation mechanism associated with the flapping motion. Fujita & Iima (2023b) considered the motion of a translating two-dimensional wing from the rest state to obtain the fundamental vortex dynamics in an unsteady wing motion. In the case of a flat wing, a secondary vortex with the opposite sign to that of the LEV, the  $\lambda$  vortex, is generated on the wing (Eldredge & Jones 2019). The  $\lambda$  vortex is interpreted to repel the LEV and play a role in releasing the LEV (Fujita & Iima 2023b; Rival *et al.* 2014).

In the case of a corrugated wing, Fujita & Iima (2023a,b) suggested that the  $\lambda$  vortex col-

lapses owing to the non-smooth structure of the corrugated wing, and the wing performance may be improved by the following two dynamic factors. The first factor is the destruction of the negative contribution to LEV release. When the  $\lambda$  vortex collapses and is stuck inside the V-shaped region of the corrugated wing, it no longer affects the LEV. Consequently, the LEVs are sequentially produced to interact with each other. This interaction guided the LEVs to move closer to the wing, leading to the formation of a low-pressure region. When the  $\lambda$  vortices are stuck imperfectly, they erupt from the V-shaped structures to the bulk and contribute to the release of LEVs. This process leads to reduced aerodynamic performance. The second factor is the strong negative pressure generated by the two alternating vortices inside the V-shaped region, a negative vortex generated from the LEV, and a positive vortex generated from the  $\lambda$  vortex. Consequently, on average, a stronger negative-pressure region is formed inside the V-shaped region. Therefore, the vortex dynamics owing to the corrugated wing structure contribute to the wing performance.

Although these mechanisms have been proposed, Fujita & Iima (2023b) investigated only the case of a single Reynolds number,  $Re = 4000$ . Therefore, it is crucial to determine the effective range of the Reynolds numbers for these mechanisms. In particular, as the Reynolds number decreases, the viscous effects become dominant, and the lift enhancement mechanisms may vanish.

The flapping flight of insects is characterised by vortex generation from the wing motion and subsequent interactions. Consequently, the dependence of these mechanisms on Reynolds number has been widely analysed. In the horizontal flapping of a flat wing, the LEV and trailing-edge vortex are shed above a critical Reynolds number within the range  $32 < Re < 64$  (Miller & Peskin 2004). For dragonfly-type two-dimensional hovering, Wang (2000) reported that the lift remains approximately constant at  $Re > 157$ . The vortex generation mechanism differs for the dragonfly wings at  $Re = 200$  and  $1000$  (Wang & Russell 2007). In elliptical wing models, vortices dissipate more rapidly at low Reynolds numbers ( $Re = O(10^3)$ ) owing to viscous effects, which may affect flight performance (Tang *et al.* 2008). A symmetric flapping model with centroidal motion exhibits asymmetric motion beyond a certain Reynolds number ( $50 < Re < 55$ ) (Ota *et al.* 2012). A modified drosophila wing model undergoing constant-velocity rotational motion showed a vortex with the opposite sign to the LEV for  $120 \leq Re \leq 1500$  (Harbig *et al.* 2013). Furthermore, some studies suggested that generating lift through vortices induced by insect flapping is challenging at  $Re < 100$  (Dudley 2002). Therefore, analysing the effective range of lift generation mechanisms in the range of several hundred to a few thousand Reynolds numbers is essential for understanding insect flight dynamics.

The aerodynamic performances of corrugated wings at low Reynolds numbers ( $Re \leq 10\,000$ ) have been extensively investigated. Zhang *et al.* (2015) numerically analysed corrugated wings based on the model ‘‘Profile 2’’ in Kesel (2000) for  $500 \leq Re \leq 12\,000$ . Their results demonstrated an improved lift-to-drag ratio compared to flat wings; however, a steady flow was not maintained as the Reynolds number increased. Similarly, Ansari *et al.* (2019) compared a wing model derived from the model ‘‘Profile 2’’ in Kesel (2000) with a NACA-profiled aerofoil at  $Re = 150$ ,  $1400$ ,  $6000$ , and  $10\,000$ , observing LEV shedding at  $Re = 1400$ , which was absent at  $Re = 150$ .

Vargas *et al.* (2008) reported that at low AoA and  $Re < 5000$ , the aerodynamic performance of corrugated wings was comparable to or worse than that of flat wings. For  $Re > 5000$  and the AoA of  $5^\circ$ , large separation regions appeared on the wing surface, whereas for  $Re \leq 5000$ , the flow remained mostly attached. A comparison between  $Re = 5000$  and  $Re = 10\,000$  indicated that the separation regions became less extensive with increasing Reynolds numbers. Meng & Sun (2011) and Meng & Sun (2013) employed the model in Rees (1975) to study gliding insects ( $35 \leq Re \leq 3000$ ) and observed a reduced lift at

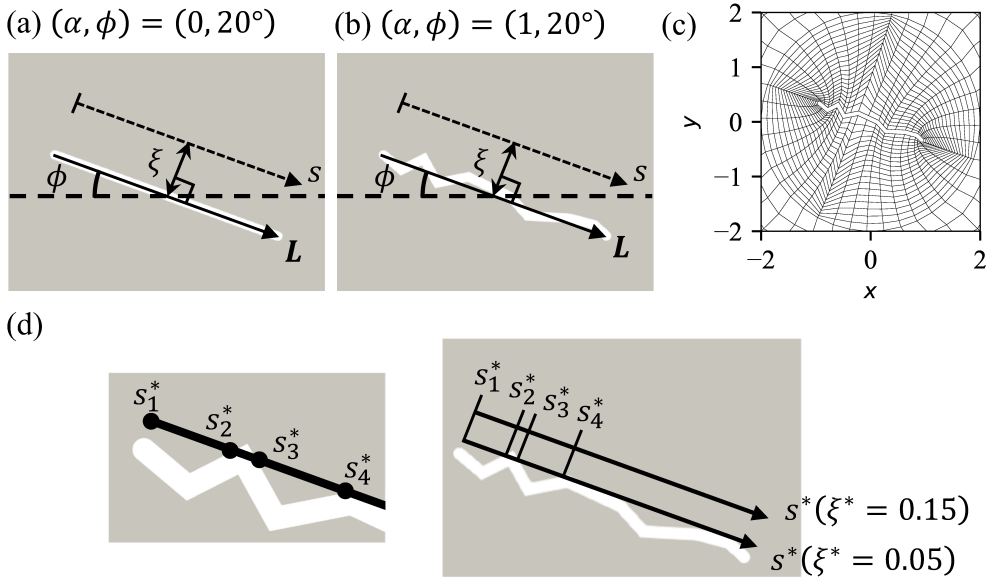


Fig 1: Wing models. (a) A flat wing ( $\alpha = 0$ ). (b) A corrugated wing ( $\alpha = 1$ ). (c) Spectral elements around the corrugated wing model ( $\phi = 20^\circ$ ). (d) The positions,  $s_1^*$ ,  $s_2^*$ ,  $s_3^*$ , and  $s_4^*$  in two cases of  $\xi^* = 0.05$  and  $0.15$  of  $(\alpha, \phi) = (1, 20^\circ)$ .

low AoA ( $15^\circ$ - $25^\circ$ ), although this effect diminished at lower Reynolds numbers. Moreover, their study showed consistent lift generation mechanisms at  $Re = 200, 1000$ , and  $2400$ . Luo & Sun (2005), using a model similar to that in Rees (1975), performed numerical analyses for  $200 \leq Re \leq 3500$  and concluded that the aerodynamic performance and flow fields of corrugated wings were largely similar to those of flat wings, regardless of the Reynolds number.

These studies suggest that the unsteady flow behaviour around corrugated wings depends on the local Reynolds numbers defined by the detailed surface flow and length scales. The vortex dynamics induced by the corrugated structures likely play a crucial role in the lift enhancement mechanisms of such wings.

In this study, we investigated the Reynolds number dependency of the wing performance of corrugated wing. We numerically calculated the flow pattern using Reynolds numbers  $100 \leq Re \leq 4000$ . For  $100 \leq Re < 1000$ , the flow patterns around the flat and corrugated wings were almost the same, and the aerodynamic performance did not depend on the wing shape. For  $1000 \leq Re < 2000$ , not the collapse of the  $\lambda$  vortex but the two alternating vortices in the V-shaped region are related to the improvement in the aerodynamic performance. For  $2000 \leq Re$ , the collapse of the  $\lambda$  vortex (Fujita & Iima 2023a,b) is related to an improvement in the aerodynamic performance. These Reynolds-number regimes are characterised by the local Reynolds number of the V-shaped region of the corrugated wing,  $Re_V$ .

## 2. Method

### 2.1. Models

A corrugated wing model was constructed based on a real-life dragonfly wing (*Aeshna cyanea*) (Kesel (2000), Profile 1). A two-dimensional wing model was generated based on a cross-section with a plane vertical to the line between the wing base and wing tip. This

position is approximately 30% from the wing base. Subsequently, a corrugated wing model was constructed by connecting the above coordinates with the line segments, commencing from the leading edge in sequence, and incorporating the thickness. We define a structural parameter  $\alpha$ , where  $\alpha = 0$  and 1 correspond to a flat wing (figure 1 (a)) and a corrugated wing (figure 1 (b)), respectively. We also define the vector  $\mathbf{L}$  that connects the two ends of the connected line segments, which are the centres of the wing (from the leading and trailing edges). The wing chord length,  $c = |\mathbf{L}|$ , was 2. The relative thickness of the wing,  $w/c$ , was 0.04, where  $w$  is the thickness of the line segments. The angle between the  $\mathbf{L}$  and  $x$  axes is defined as the AoA and is denoted by  $\phi$ . Additional construction details are provided in Fujita & Iima (2023b).

## 2.2. Numerical Simulation

The two-dimensional incompressible Navier-Stokes equations, non-dimensionalised using the free-stream velocity  $U_{\text{free}}$  and characteristic length  $c$ , are expressed as follows:

$$\frac{\partial \mathbf{u}^*}{\partial t^*} + (\mathbf{u}^* \cdot \nabla^*) \mathbf{u}^* = \nabla^* p^* + \frac{1}{Re} \Delta^* \mathbf{u}^*, \quad \nabla^* \cdot \mathbf{u}^* = 0. \quad (2.1)$$

where  $\mathbf{u}^* = (u^*, v^*)$  denotes the velocity vector and  $p^*$  represents the pressure. The Reynolds number is defined by  $Re = \frac{c U_{\text{free}}}{\nu}$ , where  $\nu$  is the kinematic viscosity. Note that non-dimensional variables are represented by the superscript  $*$ .

The spectral element method was used for the numerical calculations (Patera 1984). The computational domain was divided into quadrilateral elements, with physical quantities represented by polynomial functions to ensure ( $C^0$ ) continuity across element boundaries (Karniadakis et al. 2005). This method combines the exponential (spectral) error convergence of global collocation approaches with the geometric flexibility of standard low-order finite-element techniques (Blackburn et al. 2019). The computational software *Semtex* (Blackburn et al. 2019) was used to solve (2.1).

The calculation methods are similar to those described in Fujita & Iima (2023b). An overview is as follows. The computational domain was  $[-15, 15] \times [-15, 15]$ , with the wing model centred at  $(0, 0)$ . The outer edges of the computational domain, except for the right side ( $x^* = 15, -15 \leq y^* \leq 15$ ), were designated as inflow boundaries with  $\mathbf{u}^* = \mathbf{U}^*(t^*)$ , where  $\mathbf{U}^*(t^*) = (0, 0)$  for  $(t^* < 0)$  and  $\mathbf{U}^*(t^*) = (1, 0)$  for  $(t^* > 0)$ . The outflow conditions on the right side were applied in the same manner as those described in Fujita & Iima (2023b). This investigation sets the values of  $\nu$ , resulting in the Reynolds numbers  $100 \leq Re \leq 4000$ . The results for  $Re = 4000$  are the same as those obtained in our previous study (Fujita & Iima 2023b). The time step  $\Delta t^*$  was fixed at  $2.0 \times 10^{-5}$ , and the computations were performed within the range  $0 \leq t^* \leq 4$ .

Figure 1 (c) shows the spectral elements surrounding the corrugated wing model at the AoA of  $\phi = 20^\circ$ . The total number of spectral elements was  $N = 2960$ , with discretization of each spectral element using an  $N_p \times N_p = 19 \times 19$  mesh. Therefore,  $N_p$  denotes the number of points along the edges of each element. The verification is described in Fujita & Iima (2023b).

## 2.3. Evaluation of Aerodynamic Performance

As the relative differences in the drag coefficients were approximately the same for the AoA ( $20^\circ \leq \phi \leq 45^\circ$ ) at  $Re = 4000$  (Fujita & Iima 2023b), the aerodynamic performance was evaluated using only the lift coefficient  $C_L(\alpha, \phi, Re, t^*) = L / [(1/2) \rho c U_{\text{free}}^2]$ , where  $L$  represents the lift. The mean lift coefficients within the time interval  $[t_1^*, t_2^*]$ , denoted by

$C_{L,\text{mean}}(\alpha, \phi, Re)$ , are defined as follows:

$$C_{L,\text{mean}}(\alpha, \phi, Re) = \frac{1}{t_2^* - t_1^*} \int_{t_1^*}^{t_2^*} C_L(\alpha, \phi, Re; t^*) dt^*. \quad (2.2)$$

In particular, the lifts of corrugated and flat wings were compared. The relative difference in  $C_{L,\text{mean}}$  between the corrugated wing ( $\alpha = 1$ ) and the flat wing ( $\alpha = 0$ ),  $\Delta_{\text{mean}}$ , is defined as follows:

$$\Delta_{\text{mean}}(\phi, Re) = \frac{C_{L,\text{mean}}(1, \phi, Re) - C_{L,\text{mean}}(0, \phi, Re)}{C_{L,\text{mean}}(0, \phi, Re)}. \quad (2.3)$$

In this study,  $\Delta_{\text{mean}}$  was used as an indicator of wing performance. If  $\Delta_{\text{mean}} = 0$ , the wing performances of the corrugated and flat wings are comparable. In addition, if  $\Delta_{\text{mean}} > 0$ , the wing performance of the corrugated wing is better than that of the flat wing.

The vorticity is defined by  $\omega_z^* = \partial v^*/\partial x^* - \partial u^*/\partial y^*$ . We analysed the spatiotemporal distribution of the vorticity in a specific region near the upper surface of the wing model. This region is characterised by a distribution on a line segment defined by a shifted vector of  $\mathbf{L}$  by  $\xi$  in which  $\xi \perp \mathbf{L}$  (as shown in figures 1 (a) and (b)). The position along this line segment is described by  $s$ . Both the shift magnitude  $|\xi|$  and parameter  $s$  are normalised by the chord length of the wing, leading to the dimensionless parameters  $\xi^* = \frac{|\xi|}{c}$  and  $s^* = \frac{s}{c}$ . When  $\xi^* = 0$ ,  $s^* = 0$  and 1 correspond to the leading and trailing edges, respectively.

In this study, we examined the flow characteristics of the two cases,  $\xi^* = 0.05$  and 0.15, based on the specific flow features discussed in the following section. To specifically examine the flow characteristics near the leading edge (figure 1 (d)), we define  $(s_1^*, s_2^*, s_3^*, s_4^*) = (0.000, 0.144, 0.188, 0.353)$  and use these values in the discussion (§3.4 - §3.6). Figure 1 (d) shows their positions,  $s_1^*$ ,  $s_2^*$ ,  $s_3^*$ , and  $s_4^*$ , for  $(\alpha, \phi) = (1, 20^\circ)$ , for both  $\xi^* = 0.05$  and 0.15. For  $\xi^* = 0.05$ ,  $s_2^*$ ,  $s_3^*$ , and  $s_4^*$  represent the intersection points of the  $s^*$  axis with the wing model and the same values are used for  $\xi^* = 0.15$ .

The following subsections focus on period,  $[t_1^*, t_2^*] = [0.50, 3.25]$  (c.f. figure 2). This period corresponds to the development of the LEV and the  $\lambda$  vortex generated on the upper wing surface, including vortex collapse and interactions before the vortices detach near the wing (Fujita & Iima 2023b).

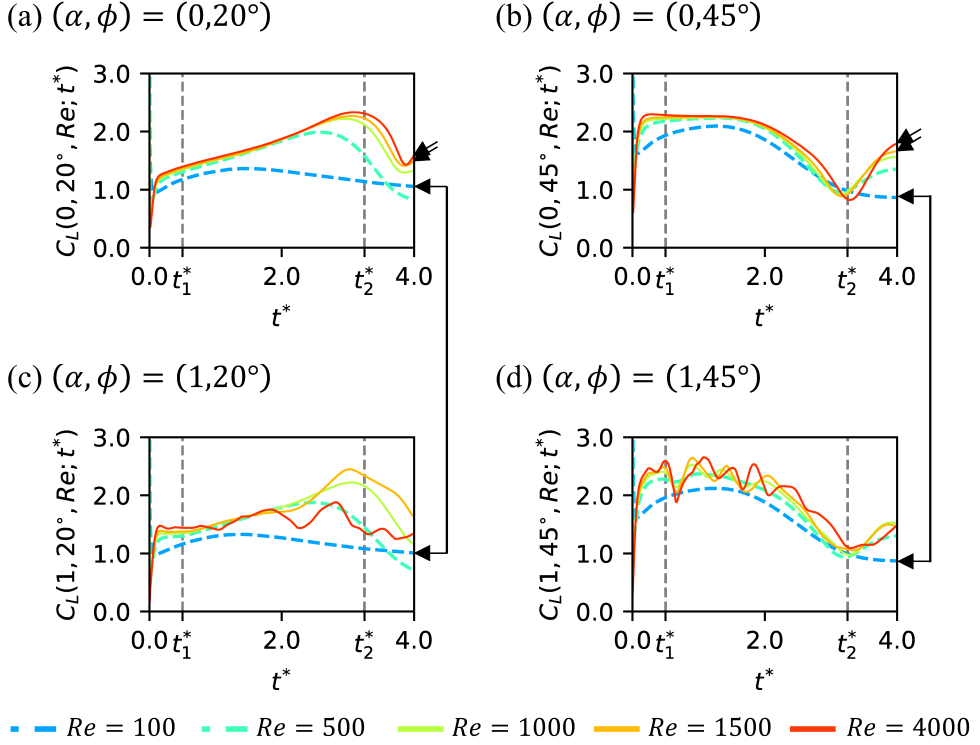


Fig 2: Time series of  $C_L(\alpha, \phi, Re; t^*)$  for the Reynolds numbers, respectively. (a)  $(\alpha, \phi) = (0, 20^\circ)$ , (b)  $(\alpha, \phi) = (0, 45^\circ)$ , (c)  $(\alpha, \phi) = (1, 20^\circ)$ , and (d)  $(\alpha, \phi) = (1, 45^\circ)$ .

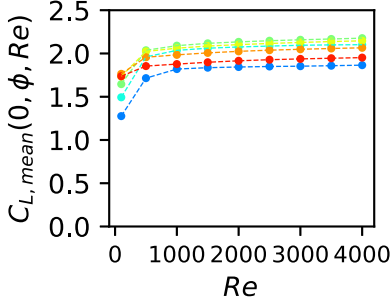
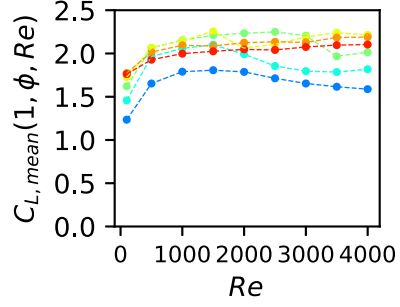
### 3. Results and discussion

#### 3.1. Reynolds number dependency of $C_L$

Figure 2 shows the time series of the lift coefficients of flat and corrugated wings for  $\phi = 20^\circ$  and  $45^\circ$ .

In the case of  $Re \leq 500$  (dashed lines), the shapes of  $C_L(0, \phi, Re; t^*)$  and  $C_L(1, \phi, Re; t^*)$  are almost the same for both values of  $\phi$ .

However, in the case of  $Re \geq 1000$ , the shapes of  $C_L(\alpha, \phi, Re; t^*)$  for  $\alpha = 0$  and 1 are different. For a flat wing, the shapes of  $C_L(0, \phi, Re; t^*)$  for  $Re = 1500$  and 4000 are similar for both values of  $\phi$  (figures 2 (a) and (b)), which is consistent with the results of previous studies (Mueller 1999; Okamoto & Ebina 2016) in which the wing performance (lift coefficient) of a flat wing did not change when  $Re = O(10^3)$ . However, for the corrugated wing, there was a significant difference between  $C_L(1, \phi, 1500; t^*)$  and  $C_L(1, \phi, 4000; t^*)$  (figures 2 (c) and (d); orange and red lines).

(a) Flat wing ( $\alpha = 0$ )(b) Corrugated wing ( $\alpha = 1$ )

●  $\phi = 20^\circ$    ●  $\phi = 25^\circ$    ●  $\phi = 30^\circ$    ●  $\phi = 35^\circ$    ●  $\phi = 40^\circ$    ●  $\phi = 45^\circ$

Fig 3: Reynolds number dependency of  $C_{L,\text{mean}}(\alpha, \phi, Re)$  for  $\phi$ , respectively. (a) The flat wing ( $\alpha = 0$ ) and (b) the corrugated wing ( $\alpha = 1$ ).

Figure 3 shows the mean lift coefficient,  $C_{L,\text{mean}}(\alpha, \phi, Re)$ .

In the case of  $Re \leq 500$ ,  $C_{L,\text{mean}}(\alpha, \phi, Re)$  was also similar for both wings, which agrees with the fact that  $C_L(\alpha, \phi, Re; \dot{t}^*)$  did not differ between the wings (figure 2). This suggests that the corrugated wing structure did not affect the wing performance in this Reynolds number regime.

However, for  $Re \geq 1000$ ,  $C_{L,\text{mean}}(\alpha, \phi, Re)$  for the flat wing was almost constant for all Reynolds numbers (figure 3 (a)). This result was consistent with that of the flapping wing reported in Wang & Russell (2007). However, for a corrugated wing,  $C_{L,\text{mean}}(\alpha, \phi, Re)$  is not constant (figure 3 (b)). When the Reynolds number increases, the value of  $C_{L,\text{mean}}(\alpha, \phi, Re)$  decreases slightly ( $\phi = 20^\circ$ ; blue line) or varies noticeably ( $\phi = 25^\circ$  and  $30^\circ$ ; figure 3 (b)). In terms of  $C_{L,\text{mean}}$ , the effect of the corrugated wing structure is apparent above  $Re = 1000$ .

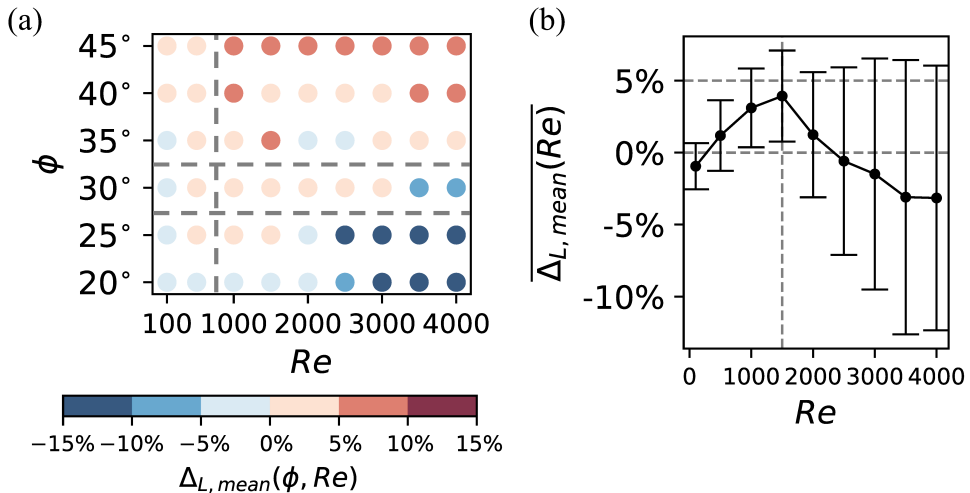


Fig 4: (a)  $\Delta_{\text{mean}}(\phi, Re)$  for the Reynolds numbers and  $\phi$ s. (b) Reynolds number dependency of average of  $\Delta_{\text{mean}}(\phi, Re)$  for  $\phi$ . Error bars indicate standard deviation.

### 3.2. Reynolds number dependency of $\Delta_{\text{mean}}$

A more detailed comparison of the aerodynamic performance of the flat and corrugated wings is shown in figure 4 (a), which illustrates the relative aerodynamic performance of the corrugated wing  $\Delta_{\text{mean}}(\phi, Re)$ . When  $\phi > 30^\circ$ ,  $\Delta_{\text{mean}}(\phi, Re)$  is positive in almost all cases, indicating an improved aerodynamic performance of the corrugated wing. However, when  $\phi < 30^\circ$ ,  $\Delta_{\text{mean}}(\phi, Re)$  is negative in almost all cases, indicating no improvement in the aerodynamic performance. Therefore, the transition of  $\Delta_{\text{mean}}(\phi, Re)$  is made around  $\phi = 30^\circ$ .

For  $Re < 1000$ , the absolute value of  $\Delta_{\text{mean}}(\phi, Re)$  is small ( $|\Delta_{\text{mean}}(\phi, Re)| < 0.04$ ) regardless of  $\phi$ , which indicates no significant difference in performance. However, as the Reynolds number increases, the absolute value of  $\Delta_{\text{mean}}(\phi, Re)$  tends to increase, confirming the difference in aerodynamic performance. For example, at  $\phi = 45^\circ$ ,  $\Delta_{\text{mean}}(45^\circ, Re) < 0.05$  for  $Re \leq 500$ , but  $\Delta_{\text{mean}}(45^\circ, Re) > 0.05$  for  $Re \geq 1000$ . By contrast, at  $\phi = 20^\circ$ ,  $\Delta_{\text{mean}}(20^\circ, Re) > -0.05$  for  $Re \leq 2000$ , but  $\Delta_{\text{mean}}(20^\circ, Re) < -0.05$  for  $Re \geq 2500$ . The results suggest that the Reynolds number at which the performance differences between flat and corrugated wings become significant depends on  $\phi$ .

For each Reynolds number, the mean value of  $\Delta_{\text{mean}}(\phi, Re)$  for  $20^\circ \leq \phi \leq 45^\circ$  was defined as  $\overline{\Delta_{\text{mean}}(Re)}$ . Figure 4 (b) shows  $\overline{\Delta_{\text{mean}}(Re)}$ . For  $100 \leq Re \leq 1500$ ,  $\overline{\Delta_{\text{mean}}(Re)}$  increases with the Reynolds number. However, for  $1500 \leq Re \leq 4000$ ,  $\overline{\Delta_{\text{mean}}(Re)}$  decreased as the Reynolds number increased. Therefore, the mean aerodynamic performance of the corrugated wing was optimised at  $Re = 1500$ , which is consistent with the findings of Fujita & Iima (2023a). The error bars in figure 4 (b) represent the standard deviation (SD). The smallest SD was observed at  $Re = 100$ . For  $Re \leq 3500$ , the SD increased monotonically with the Reynolds number, and the SD at  $Re = 4000$  was slightly smaller but similar to that at  $Re = 3500$ .

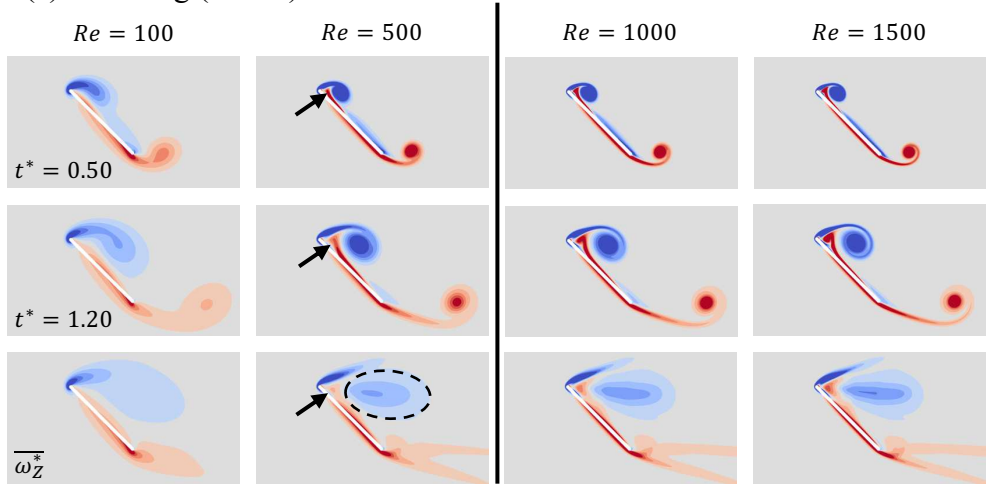
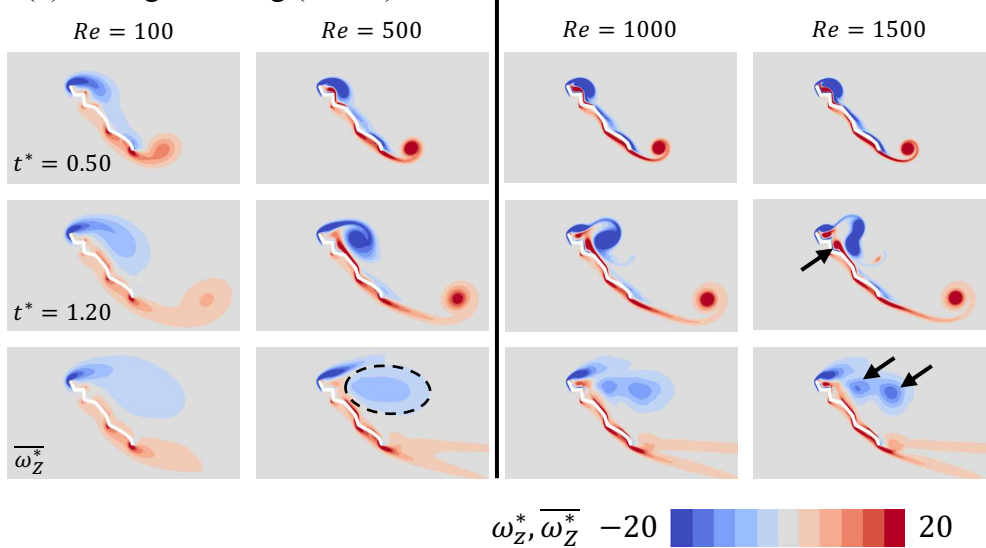
(a) Flat wing ( $\alpha = 0$ )(b) Corrugated wing ( $\alpha = 1$ )

Fig 5: Vorticity fields around wings for  $\phi = 45^\circ$  at  $Re = 100, 500, 1000,$  and  $1500$ . The first row and the second row display snapshots at  $t^* = 0.50$  and  $t^* = 1.20$ , respectively. The third row shows the mean vorticity field,  $\overline{\omega_z^*}$  in  $[t_1^*, t_2^*]$ . (a) The flat wing ( $\alpha = 0$ ) and (b) the corrugated wing ( $\alpha = 1$ ).

## 3.3. Vortex pattern

3.3.1. In the case of  $\phi = 45^\circ$ 

In order to compare the flow patterns associated with the improved aerodynamic performance of the corrugated wing, the vorticity fields around the wings for  $\phi = 45^\circ$  at  $Re = 100, 500, 1000,$  and  $1500$  are shown in figure 5. Figures 5 (a) and (b) show the vorticity fields around flat and corrugated wings, respectively. The first and second rows show snapshots at  $t^* = 0.50$  and  $t^* = 1.20$ , respectively. The third row presents the mean vorticity field,  $\overline{\omega_z^*}$  over  $[t_1^*, t_2^*]$ .

For the flat wing (figure 5 (a)), the vortex at  $t^* = 0.50$  grew in a self-similar manner

regardless of the Reynolds number. At  $Re = 100$ , a large region of negative vorticity corresponding to the LEV forms above the wing. As the Reynolds number increased, the LEV became more pronounced and exhibited a circular structure. Adjacent to the LEV, a vortex with positive vorticity, identified as the  $\lambda$  vortex, was observed (see the arrows for  $Re = 500$ ). This  $\lambda$  vortex grows and erupts between two LEVs when one LEV is released (Rival et al. 2014; Eldredge & Jones 2019; Fujita & Iima 2023b).

For the mean vorticity fields at  $Re = 500, 1000$ , and  $1500$ , an elongated region of negative vorticity is observed along the upper surface of the wing (dashed ellipse for  $Re = 500$ ). This elongation resulted from the advection of the LEV downstream. The magnitude of this negative vorticity increased monotonically with the Reynolds number. Furthermore, a positive vorticity distribution was observed between the leading-edge negative vorticity and the elongated negative vorticity region on the upper surface, which was attributed to the eruption of the  $\lambda$  vortex (see arrow for  $Re = 500$ ).

For the corrugated wing (figure 5 (b)), the vortex at  $t^* = 0.50$  also grew in a self-similar manner at  $Re = 100$  and  $500$ , similar to the flat wing case. However, at  $Re = 1000$  and  $1500$ , vortex growth did not exhibit self-similarity. Specifically, the positive vortex splits into multiple smaller vortices, which become stuck in the V-shaped regions (arrow for  $Re = 1500$ ). This indicates the collapse of the  $\lambda$  vortex owing to the corrugated structure. Additionally, the two LEVs were aligned side by side above the wing, which is consistent with the observations at  $Re = 4000$  (Fujita & Iima 2023b).

For the mean vorticity field at  $Re = 500$ , an elongated negative vorticity distribution appears along the upper surface (dashed ellipse), similar to the flat-wing case (figure 5 (a)). However, at  $Re = 1000$  and  $1500$ , two distinct negative vorticity regions were formed above the wing (arrows for  $Re = 1500$ ). This was because the fully separated LEV moved above the corrugated wing in an isolated state.

Comparing the results for both wings (figures 5 (a) and (b)), we note that as the Reynolds number increases, the vortex dynamics around the corrugated wing differ from those around the flat wing above  $Re \geq 1000$ . As a result of the transition of vortex dynamics in the corrugated wing, its aerodynamic performance of the corrugated wing improved (figure 4). Specifically, the collapse of the  $\lambda$  vortex and interaction between the two LEVs caused the LEV to move closer to the corrugated wings. Because the vortex centre corresponds to the region of negative pressure, the negative pressure distribution on the corrugated wing surface becomes wider than that on the flat wing (data not shown; refer to Fujita & Iima (2023b)). Consequently, the aerodynamic performance of the corrugated wing was better than that of a flat wing. Therefore, the vortex dynamics are strongly associated with the lift enhancement mechanism of corrugated wings.

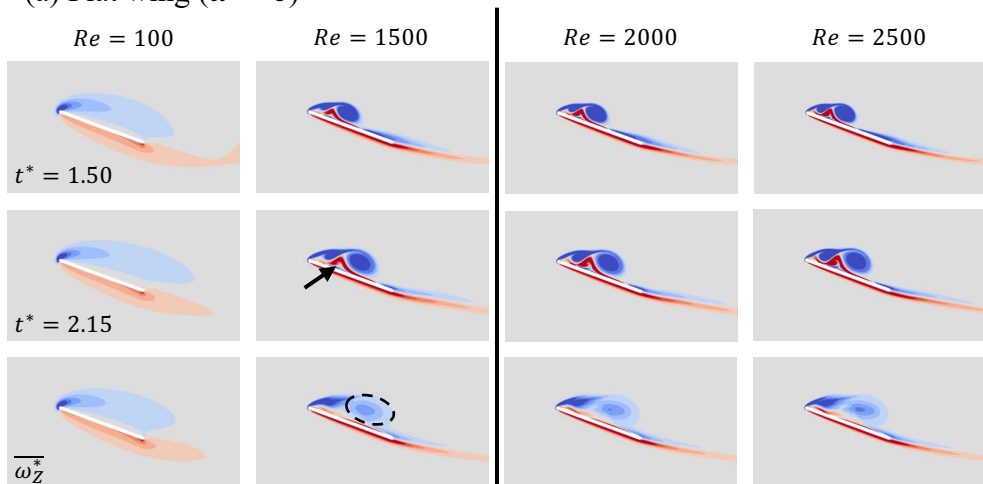
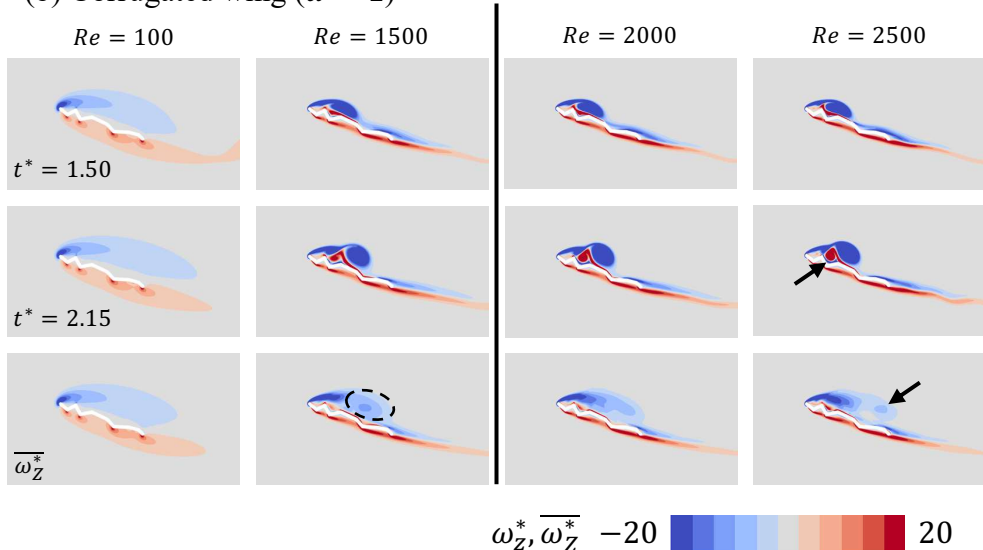
(a) Flat wing ( $\alpha = 0$ )(b) Corrugated wing ( $\alpha = 1$ )

Fig 6: Vorticity fields around wings for  $\phi = 20^\circ$  at  $Re = 100, 1500, 2000,$  and  $2500$ . The first row and the second row display snapshots at  $t^* = 1.50$  and  $t^* = 2.15$ , respectively.

The third row shows the mean vorticity field,  $\overline{\omega_z^*}$ . (a) The flat wing ( $\alpha = 0$ ) and (b) the corrugated wing ( $\alpha = 1$ ).

### 3.3.2. In the case of $\phi = 20^\circ$

To compare the flow patterns in the cases where the aerodynamic performance of the corrugated wing did not improve, the vorticity fields around the wings at  $\phi = 20^\circ$  and  $Re = 100, 1500, 2000,$  and  $2500$  are shown in figure 6. Figures 6 (a) and (b) show the vorticity fields around the flat and corrugated wings, respectively. The first and second rows show snapshots at  $t^* = 1.50$  and  $t^* = 2.15$ , respectively, and the third row depicts the mean vorticity field,  $\overline{\omega_z^*}$  over  $[t_1^*, t_2^*]$ .

For the flat wing (figure 6 (a)), the vortex at  $t^* = 1.50$  exhibits self-similar growth across

all Reynolds numbers, similar to the case of  $\phi = 45^\circ$  (figure 5 (a)). At  $Re = 100$ , a large region of negative vorticity corresponding to the LEV forms above the wing. As the Reynolds number increases, the LEV becomes more pronounced and maintains its circular structure. A positive vorticity region, identified as the  $\lambda$  vortex, appeared adjacent to the LEV (arrow at  $Re = 1500$ ).

In addition, for the mean vorticity field at  $\phi = 20^\circ$ , the flow patterns are similar to those in the case of  $\phi = 45^\circ$  (figure 5 (a)). However, unlike the  $\phi = 45^\circ$  case, the LEV moved near the wing surface, preventing a distinct  $\lambda$  vortex distribution. This led to a more concentrated negative vorticity region near the wing.

For the corrugated wing (figure 6 (b)), the vortex at  $t^* = 1.50$  grew in a self-similar manner to that at  $Re = 100$ , similar to the flat wing. At  $Re = 1500$ , although the vortices at  $t^* = 1.50$  are not similar to the flat wing, the shape of the  $\lambda$  vortex at  $t^* = 2.15$  is similar. Therefore, we consider the vortex to grow in a self-similar manner (refer to the mean vorticity field and figure 8). However, at  $Re = 2000$  and  $2500$ , vortex growth did not exhibit self-similarity. At  $t^* = 2.15$ , a positive vortex with a more rounded shape is observed adjacent to the two LEVs (arrow at  $Re = 2500$ ), indicating the  $\lambda$ -vortex eruption due to the corrugated structure. This phenomenon was observed for  $Re \geq 2000$  and was consistent with the observations at  $Re = 4000$  (Fujita & Iima 2023b).

For the mean vorticity field at  $Re = 100$  and  $1500$ , the flow patterns were similar to those of the flat-wing case (figure 6 (a)). However, at  $Re = 2000$ , this distribution is not present. At  $Re = 2500$ , a single distinct negative vorticity region was observed above the wing (arrow), in contrast to the two separate regions observed at  $\phi = 45^\circ$  (figure 5 (b)). This suggests that the  $\lambda$ -vortex eruption caused the LEV to move further from the wing, thereby weakening the vorticity distribution (Fujita & Iima 2023b).

Comparing both the wings (figures 6 (a) and (b)), we observe that the vortex dynamics around the corrugated wing deviate from those of the flat wing in  $Re > 1500$ . Although  $|\Delta_{\text{mean}}(20^\circ, 2000)| = |-0.031| < 0.05$  (figure 4 (a)), the flow begins to exhibit changes at  $Re = 2000$ . As the Reynolds number increased, the  $\lambda$  vortex erupted, causing the LEV to move away from the corrugated wing. This reduces the lift enhancement mechanism observed at  $\phi = 45^\circ$  and results in no significant improvement in the aerodynamic performance (Fujita & Iima 2023b).

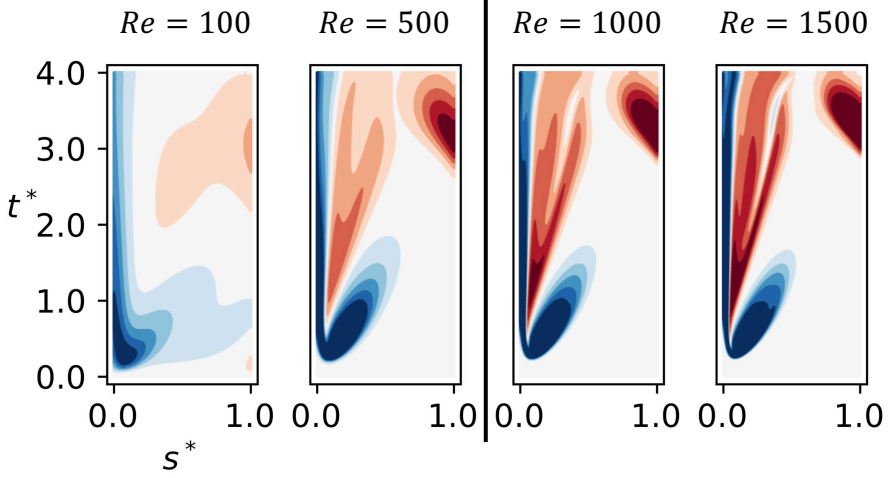
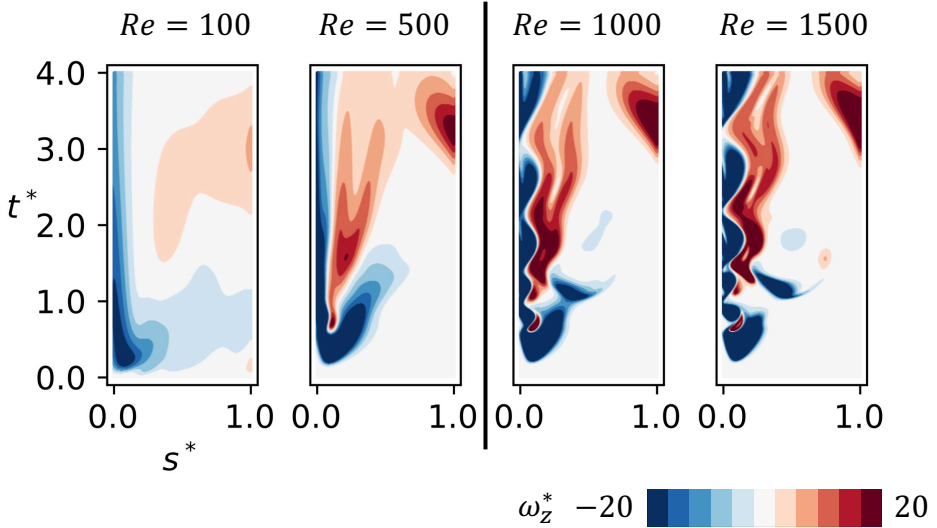
(a) Flat wing ( $\alpha = 0$ )(b) Corrugated wing ( $\alpha = 1$ )

Fig 7: Spatio-temporal distribution of  $\omega_z^*$  on  $\xi^* = 0.15$  for  $\phi = 45^\circ$ . Conditions are the same as figure 5.

### 3.3.3. Spatio-temporal distribution of $\omega_z^*$ on $\xi^* = 0.15$

Next, the spatio-temporal flow pattern of the flat wing was compared with that of the corrugated wing for different Reynolds numbers ( $\phi = 45^\circ$ ). Figure 7 shows the spatio-temporal distribution of the vorticity along the  $s^*$  axis at  $\xi^* = 0.15$ . Figures 7 (a) and (b) show the results for flat and corrugated wings, respectively. At  $Re = 100$  and  $500$ , the vortex pattern of the flat wing was almost the same as that of the corrugated wing. At  $Re = 1000$  and  $1500$ , the vortex patterns of these wings differ substantially, particularly in the region near the leading edge (small values of  $s^*$ ); an oscillation is observed (e.g. figure 7 (b);  $Re = 1500$ ). Because we focused on the distribution on  $\xi^* = 0.15$  at a distance away from the V-shaped region, the alternation of vortices was represented by an oscillation.

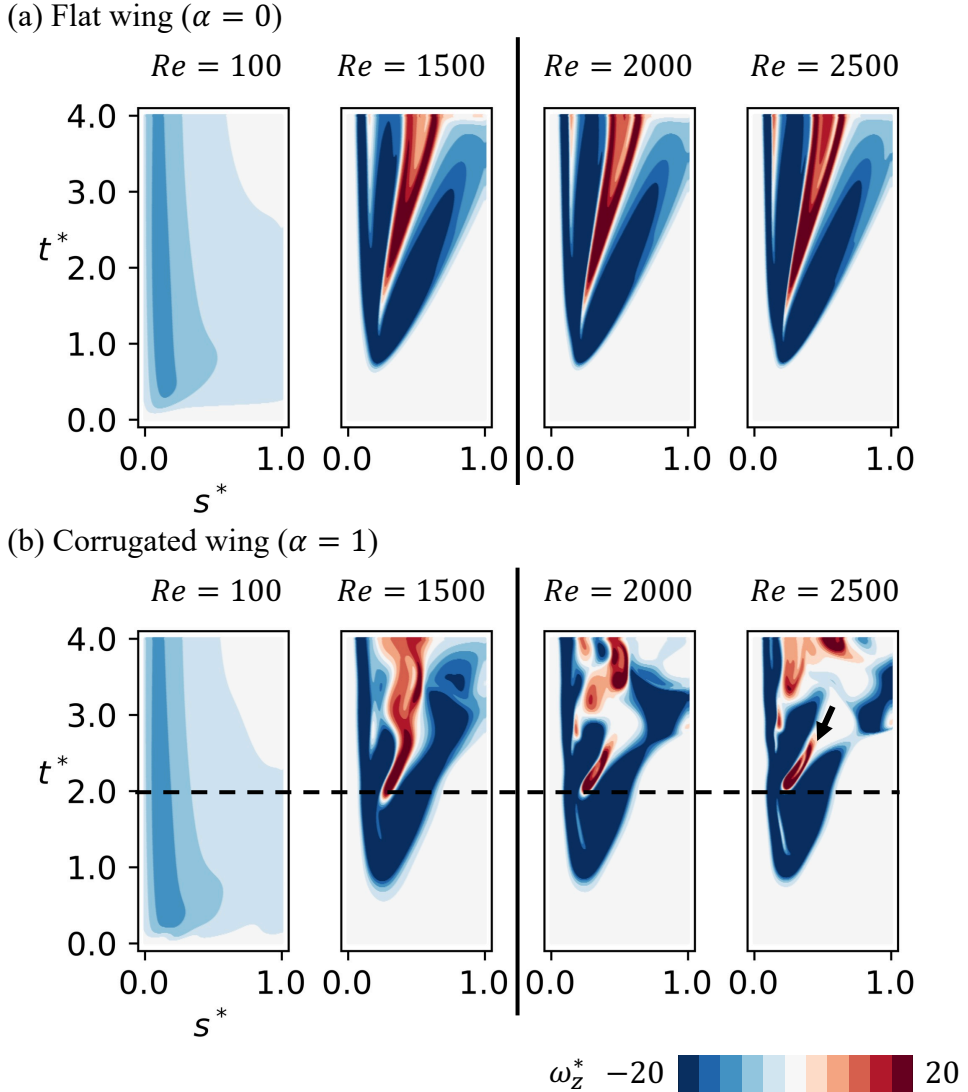


Fig 8: Spatio-temporal distribution of  $\omega_z^*$  on  $\xi^* = 0.15$  for  $\phi = 20^\circ$ . Conditions are the same as figure 6.

Figures 8 (a) and (b) show the spatio-temporal distribution of vorticity along the  $s^*$  axis at  $\xi^* = 0.15$  ( $\phi = 20^\circ$ ) for a flat wing and corrugated wing, respectively. At  $Re = 100$ , the vortex patterns of both wings are similar to those in  $\phi = 45^\circ$ . At  $Re = 1500$ , the vortex pattern of the flat wing is qualitatively similar to that of the corrugated wing, although a slight oscillation in the positive vorticity region is observed. At  $Re = 2000$  and  $2500$ , the vortex patterns on the wings differ substantially. In addition, the  $\lambda$ -vortex eruption is represented as a vorticity region with a positive sign (red) around  $(s^*, t^*) = (0.25, 2)$  at  $(\alpha, \phi, Re) = (1, 20^\circ, 2500)$ , which indicates advection towards the trailing edge (in the direction of increasing  $s^*$ ) (figure 8 (b);  $Re = 2500$ , arrow). However, such features were not observed when the wing performance

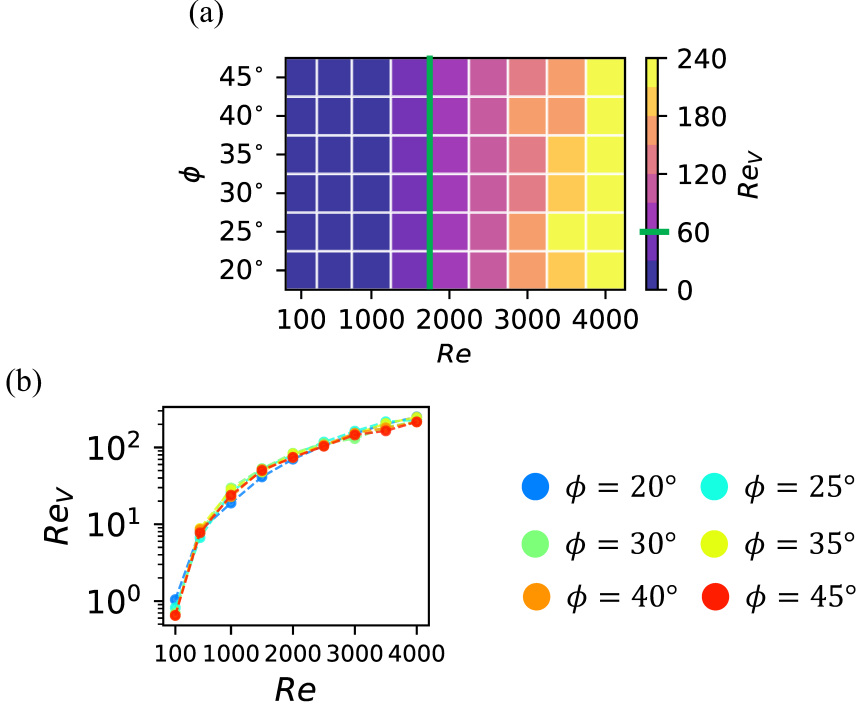


Fig 9: (a)  $Re_V$  for  $20^\circ \leq \phi \leq 45^\circ$  and  $100 \leq Re \leq 4000$ . (b) Reynolds number dependency of  $Re_V$  for  $\phi$ , respectively. We have used a log scale on the vertical axis.

improved (figure 7 (b);  $Re = 1500$ ). The detailed mechanism is discussed in Fujita & Iima (2023b).

#### 3.4. Flow characterization near the V-shaped region

As shown in §3.3, the characteristic behaviour of vortex motion on the flat wing and that of the corrugated wing differs with increasing Reynolds number. We hypothesise that this change is attributable to the flow characteristics near the concavo-convex structure of the corrugated wing. To quantify this, we defined the local Reynolds number characterised by the V-shaped structure of the corrugated wing,  $Re_V$ , as follows:

$$Re_V := \frac{bU_V}{\nu}, \quad (3.1)$$

where  $b$  represents the characteristic depth of the V-shaped region.  $U_V$  is the characteristic flow speed in the V-shaped region. We set  $b = \frac{2}{9}$  as the aspect ratio of the corrugated wing model (figure 1 (b)), which can be approximately estimated as 9 : 1. The value of  $U_V$  was estimated from the average velocity along the line at  $\xi^* = 0.05$  as follows:

$$U_s(t^*) = \frac{1}{(s_2^* - s_1^*) + (s_4^* - s_3^*)} \left\{ \int_{s_1^*}^{s_2^*} |U(s^*, t^*)| ds^* + \int_{s_3^*}^{s_4^*} |U(s^*, t^*)| ds^* \right\}, \quad (3.2)$$

$$U_V = \frac{1}{t_2^* - t_1^*} \int_{t_1^*}^{t_2^*} U_s(t^*) dt^*.$$

Here, interval  $s_2^* < s^* < s_3^*$  was excluded because it overlapped the convex part (figure 1 (d)).

Figure 9 (a) shows  $Re_V$  for  $(\phi, Re)$ . As the Reynolds number increases,  $Re_V$  also increases; however, it is less dependent on  $\phi$ . In particular,  $Re_V \geq 60$  for  $2000 \leq Re \leq 4000$  (figure 9 (a); green line). In the range of  $2000 \leq Re \leq 4000$ , the flow fields around the corrugated wing were influenced by the corrugated structure, resulting in a deviation in the performance from the flat wing; however, the details depend on the value of  $\phi$  (figures 4 (b), 7, and 8). According to observations, the critical  $Re_V$  in this system is 60, which roughly corresponds to the vortex detachment of other flapping-wing models, c.f. Miller & Peskin (2004) and Ota *et al.* (2012). This agrees with our observation that vortex detachment ( $\lambda$ -vortex eruption or collapse) from the tip of the corrugated structure occurs at  $60 \leq Re_V$  ( $2000 \leq Re$ ).

Figure 9 (b) shows the Reynolds-number dependence of  $Re_V$  for  $\phi$ , respectively. It is shown that  $Re_V$  is a function of  $Re$  irrespective of  $\phi$ . In particular, we observe that this is  $Re_V < 10$  for  $100 \leq Re \leq 500$ . This suggests that the flow around the corrugated wing for  $100 \leq Re \leq 500$  is not significantly affected by the concavo-convex structure, which also agrees with our observations.

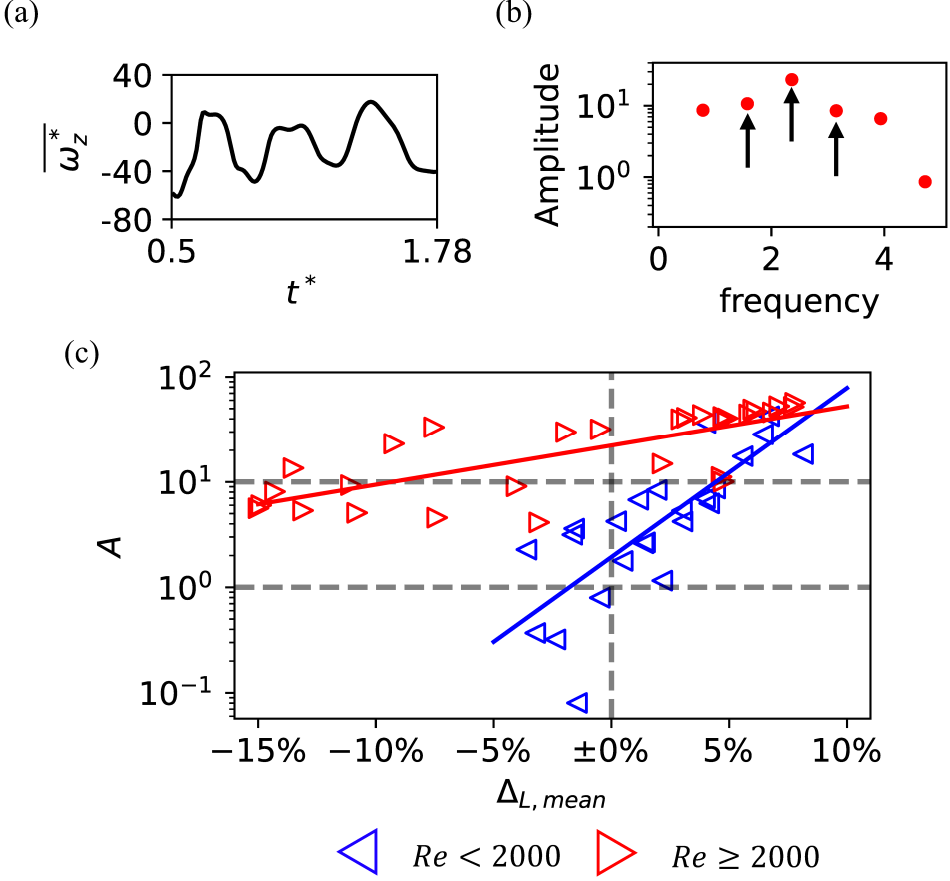


Fig 10: (a) Time series of  $\overline{\omega_z^*}$  for  $(\alpha, \phi, Re) = (1, 45^\circ, 1500)$ . (b) Results of Fourier analysis for (a). (c) Scatter plot of  $\Delta_{L, mean}$  and the amplitude of particular frequencies,  $A$ . Blue triangles indicate for the case of  $Re < 2000$ . Red triangles also indicate the case of  $Re \geq 2000$ . The straight line results from a regression curve for each Reynolds number regime, respectively.

### 3.5. Oscillation of the LEV in the leading edge

As the Reynolds number increases, the flow around the corrugated wing is influenced by the corrugated structure, resulting in the oscillation of the vortex in the V-shaped region, as observed in figure 7(b) at  $Re = 1500$ . Consequently, the oscillation enhances the aerodynamic performance of the corrugated wing, as discussed in Fujita & Iima (2023b) in the case of  $Re = 4000$ . Here, we quantified the Reynolds-number dependence of the mechanism as follows. We shifted the  $s^*$  axis to capture the oscillation of the LEV by setting  $\xi^* = 0.15$  and considered the spatiotemporal region characterised by  $0.5 \leq t^* \leq 1.78$  and  $s_1^* \leq s^* \leq s_2^*$ . The vortex behaviour is characterised as follows:

$$\overline{\omega_z^*(t^*)} = \frac{1}{s_2^* - s_1^*} \int_{s_1^*}^{s_2^*} \omega_z^*(s^*, t^*) ds^*. \quad (3.3)$$

Note that the spatial sampling region is narrower than the definition of  $U_s(t^*)$  (3.2) because we focus on the single V-shaped region containing the leading edge.

Figure 10 (a) shows a time series of  $\overline{\omega_z^*(t^*)}$  at  $(\alpha, \phi, Re) = (1, 45^\circ, 1500)$ , which succeeded in capturing the oscillation in figure 7 (b) at  $Re = 1500$ , as quantified by Fourier analysis (figure 10 (b)). In this case, the highest amplitude was observed at  $f = 2.36\text{Hz}$ . Improvements in wing performance owing to oscillation are correlated with the amplitudes observed at frequencies of  $f = 1.57\text{Hz}$ ,  $2.36\text{Hz}$  and  $3.15\text{Hz}$ . The sum of these amplitudes,  $A$ , was used to characterise the oscillation.

The scatter plots for  $\Delta_{\text{mean}}$  and  $A$  are shown in figure 10 (c). The blue triangles indicate  $Re < 2000$ . The straight blue line represents the regression curve  $A = 10^{16.08\Delta_{\text{mean}}+0.29}$  (figure 10 (c)). The improved wing performance is strongly correlated with  $A$ . Therefore, for  $Re < 2000$ , the oscillations of the LEV with a frequency of  $1.57 \leq f \leq 3.15$  improve wing performance, as demonstrated in Fujita & Iima (2023b).

For  $2000 \geq Re$ , the scatter plot is represented by red triangles (figure 10 (c)). Regardless of wing performance,  $A$  keeps relatively larger values. However, the improved wing performance is correlated with  $A$ . The regression curve in this case exhibited a lower rate of change than that in the case of  $Re < 2000$  (figure 10 (c), red line;  $A = 10^{3.73\Delta_{\text{mean}}+1.35}$ ).

In summary, for  $Re < 2000$ ,  $A$  has a strong correlation with  $\Delta_{\text{mean}}$ . Even for  $Re \geq 2000$ , there is a correlation with  $\Delta_{\text{mean}}$ , although not strong. This indicates that the oscillation of the LEV at the leading edge of the corrugated wing enhanced the aerodynamic performance.

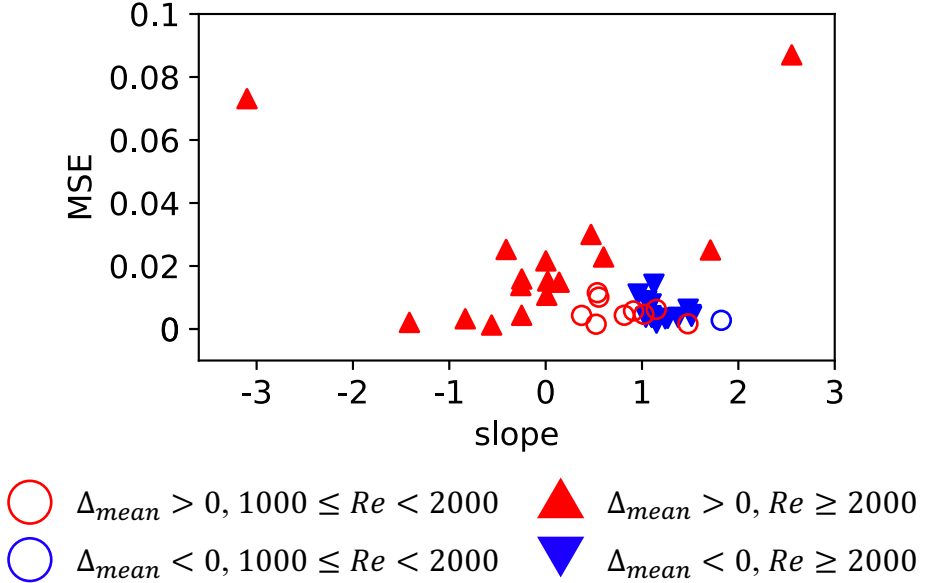


Fig 11: Scatter plot of the slope and the mean squared error for the result of pick up of the  $\lambda$ -vortex eruption for the corrugated wing ( $\alpha = 1$ ).

### 3.6. The $\lambda$ -vortex eruption

For  $2000 \leq Re \leq 4000$ , where the flow around the corrugated wing is affected by the corrugated structure, the  $\lambda$ -vortex eruption is a factor in the decrease in the aerodynamic performance of the corrugated wing. To confirm this, the analysis of the  $\lambda$ -vortex eruption performed in our previous study (Fujita & Iima 2023b) was extended to all the Reynolds numbers investigated. At  $\xi^* = 0.15$ , the points satisfying the condition that  $\omega_z^* \geq 20$  is in the range  $1.5 \leq t^* \leq 2.5$  and  $0.25 \leq s^*$  are selected, and a linear fit using the least-squares method is applied to that point group.

Figure 11 shows a scatter plot of the slope of the regression line and the mean squared error (MSE). For all values of  $\phi$  for  $Re < 1000$  and  $\phi = 20^\circ$  and  $25^\circ$  at  $Re = 1000$ , there are no points of  $\omega_z^*$  satisfying the condition.

The triangles represent the corrugated-wing data in  $Re \geq 2000$ . The blue inverted triangles represent the data for cases in which  $\Delta_{mean} < 0$  and  $2000 \leq Re$ . The regression line clusters were characterised by a constant slope and a small MSE. This corresponds to the  $\lambda$ -vortex eruption. However, when  $\Delta_{mean} > 0$  and  $Re \geq 2000$  (figure 11; red triangles), the results are scattered, which is the same trend as the results for  $Re = 4000$  (Fujita & Iima 2023b).

The circles represent the corrugated-wing data in  $1000 \leq Re < 2000$ . These points are confined to a region that overlaps that of the inverted triangles, which correspond to the decrease in wing performance due to the  $\lambda$ -vortex eruption. However, within this Reynolds number range, many of the circles indicate an increase in wing performance (highlighted in red), suggesting that the  $\lambda$ -vortex eruption does not necessarily lead to a decrease in wing performance. Consequently, it is the oscillations of the LEV that contribute to enhancing the performance of the corrugated wing.

In summary, for  $Re < 2000$ , the  $\lambda$ -vortex eruption does not affect the aerodynamic performance of the corrugated wing. However, for  $Re \geq 2000$ , the  $\lambda$ -vortex eruption was observed when the aerodynamic performance of the corrugated wing decreased.

#### 4. Concluding remarks

In this study, a two-dimensional direct numerical simulation was employed to evaluate the performance of the corrugated wing. In particular, a detailed investigation was conducted on the dependency of the Reynolds number in the regime  $100 \leq Re \leq 4000$ . Consequently, the two lift enhancement mechanisms proposed by Fujita & Iima (2023b), oscillation due to vortex alternation near the leading edge and  $\lambda$ -vortex eruption, were identified as significant mechanisms operating in different Reynolds number regions.

For  $Re < 1000$ , the corrugated structure did not contribute to the flow or wing performance (figures 4, 5, and 6), because the local Reynolds numbers inside the corrugated structures were too small for the secondary vortex to work. This result is relevant to insects such as flies and mosquitoes flying at  $Re \lesssim 100$  (Bomphrey *et al.* 2017; Zhang & Huang 2019). Their wings appear less corrugated than those of dragonflies (Sudo *et al.* 2000).

For  $1000 \leq Re < 2000$ , vortex oscillations were observed near the leading edge. When wing performance improved, oscillations with a frequency of  $1.57 \leq f \leq 3.15$  were detected (figure 10 (c)). However, no clear correlation with the  $\lambda$  vortex collapse or eruption was established because the  $\lambda$  vortex was determined to erupt at all Reynolds numbers (figure 11). This result can be attributed to the viscous effects on the  $\lambda$  vortex and LEV motions. This can be clarified further by tracking the LEV trajectory, which remains a subject for future research.

When wing performance was evaluated by the average of  $\Delta_{\text{mean}}$  over AoA,  $\overline{\Delta_{\text{mean}}(Re)}$ , it was highest at  $Re = 1500$ , whereas larger Reynolds number cases showed greater performance deviations (figure 4 (c)). This indicates that at  $Re = O(10^3)$ , the corrugated wing can generate a greater or lower lift than the flat wing by controlling the AoA. These results suggest that corrugated wings may provide better manoeuvrability than flat wings and offer insights into the flight behaviours of real dragonflies, such as foraging and escape. They could also contribute to the development of flying robots and drones.

For  $2000 \leq Re$ , the  $\lambda$  vortex contributes to wing performance (see figure 11). The detailed mechanisms have been reported and discussed in Fujita & Iima (2023a,b). Also, vortex oscillations have also been observed near the leading edge (Fujita & Iima 2023a,b). In the case of improved wing performance, oscillations in the frequency of  $1.57 \leq f \leq 3.15$  were observed more significantly; however, the correlation was milder than that in the regime  $1000 \leq Re < 2000$  (see figure 10 (c)).

The flow characteristics in these Reynolds-number regimes can be clarified using the local Reynolds number inside the V-shaped region of the corrugated wing,  $Re_V$ . In particular, the critical  $Re_V$  related to vortex shedding is  $Re_V = O(10^2)$ , which agrees with a previous study (Dudley 2002; Miller & Peskin 2004; Ota *et al.* 2012). Future studies could benefit from comparisons of vortex shedding around other objects. For example, vortex shedding from convex regions was observed at  $Re > 300$  around a triangular model on a wall as a two-dimensional dune (Fujita *et al.* 2020). Understanding the vortex motion induced by an uneven structure may provide a universal perspective.

This study focused on a single corrugated shape, and the shape dependency remains a problem to be clarified. In this study, we proposed and successfully demonstrated a quantity that represents the characteristics of the local flow,  $Re_V$ , rather than the overall flow or wing structure. This suggests that a better characterization is applicable for different corrugated shapes.

Three-dimensionality and wing-flapping motions should be done for future research. Considering these factors, flow dynamics, such as wingtip vortices, may influence the vortex dynamics presented in this paper. Quantitative analysis of these flow structures and their link to lift generation could facilitate further discussions on the hydrodynamic role of corrugated

structures and their optimisation. Studying this phenomenon under realistic conditions can answer the biological question of why many insects, including dragonflies, and support applications in robotics and other fields.

**Funding.** This work was supported by JSPS KAKENHI (19K03671, 21H05303, 22KJ2316, 24K22861), the SECOM Science and Research Foundation, and Satake fund.

**Author ORCIDs.** Authors may include the ORCID identifiers as follows. Y. Fujita, <https://orcid.org/0009-0005-6859-6749>; M. Iima, <https://orcid.org/0000-0002-1060-4604>.

**Declaration of Interests.** The authors report no conflict of interest.

## REFERENCES

- ANSARI, MOHD IMRAN, SIDDIQUE, MOHAMMED HAMID, SAMAD, ABDUS & ANWER, SYED FAHAD 2019 On the optimal morphology and performance of a modeled dragonfly airfoil in gliding mode. *Physics of Fluids* **31** (5), 051904.
- BAUERHEIM, MICHAEL & CHAPIN, VINCENT 2020 Route to chaos on a dragonfly wing cross section in gliding flight. *Physical Review E* **102** (1), 011102.
- BLACKBURN, HUGH M, LEE, D, ALBRECHT, THOMAS & SINGH, JAGMOHAN 2019 Semtex: A spectral element–fourier solver for the incompressible navier–stokes equations in cylindrical or cartesian coordinates. *Computer Physics Communications* **245**, 106804.
- BOMPHELY, RICHARD J, NAKATA, TOSHIYUKI, HENNINGSSON, PER & LIN, HUAI-TI 2016 Flight of the dragonflies and damselflies. *Philosophical Transactions of the Royal Society B: Biological Sciences* **371** (1704), 20150389.
- BOMPHELY, RICHARD J, NAKATA, TOSHIYUKI, PHILLIPS, NATHAN & WALKER, SIMON M 2017 Smart wing rotation and trailing-edge vortices enable high frequency mosquito flight. *Nature* **544** (7648), 92–95.
- CHIN, DIANA D & LENTINK, DAVID 2016 Flapping wing aerodynamics: from insects to vertebrates. *Journal of Experimental Biology* **219** (7), 920–932.
- DUDLEY, ROBERT 2002 The biomechanics of insect flight: form, function, evolution. Princeton University Press.
- ELDRIDGE, JEFF D & JONES, ANYA R 2019 Leading-edge vortices: mechanics and modeling. *Annual Review of Fluid Mechanics* **51**, 75–104.
- ELLINGTON, CHARLES PORTER 1984 The aerodynamics of hovering insect flight. iv. aerodynamic mechanisms. *Philosophical Transactions of the Royal Society of London. B, Biological Sciences* **305** (1122), 79–113.
- ELLINGTON, CHARLES P, VAN DEN BERG, COEN, WILLMOTT, ALEXANDER P & THOMAS, ADRIAN LR 1996 Leading-edge vortices in insect flight. *Nature* **384** (6610), 626–630.
- FUJITA, YUSUKE & IMA, MAKOTO 2023a Aerodynamic performance of dragonfly wing model that starts impulsively: how vortex motion works. *Journal of Fluid Science and Technology* **18** (1), JFST0013–JFST0013.
- FUJITA, YUSUKE & IMA, MAKOTO 2023b Dynamic lift enhancement mechanism of dragonfly wing model by vortex-corrugation interaction. *Physical Review Fluids* **8**, 123101.
- FUJITA, YUSUKE, NISHIMORI, HIRAKU & IMA, MAKOTO 2020 Dead-water region around two-dimensional sand-dune models. *Journal of the Physical Society of Japan* **89** (6), 063901.
- HARBIG, ROBERT RICHARD, SHERIDAN, JOHN & THOMPSON, MARK CHRISTOPHER 2013 Reynolds number and aspect ratio effects on the leading-edge vortex for rotating insect wing planforms. *Journal of Fluid Mechanics* **717**, 166–192.
- KARNIADAKIS, GEORGE EM, KARNIADAKIS, GEORGE & SHERWIN, SPENCER 2005 Spectral/hp element methods for computational fluid dynamics. Oxford University Press on Demand.
- KESEL, ANTONIA B 2000 Aerodynamic characteristics of dragonfly wing sections compared with technical aerofoils. *Journal of experimental biology* **203** (20), 3125–3135.
- LANDAU, LEV DAVIDOVICH & LIFSHITZ, EVGENII MIKHAILOVICH 2013 Fluid Mechanics: Landau and Lifshitz: Course of Theoretical Physics, Volume 6, , vol. 6. Elsevier.
- LIU, HAO, WANG, SHIZHAO & LIU, TIANSHU 2024 Vortices and forces in biological flight: Insects, birds, and bats. *Annual Review of Fluid Mechanics* **56**, 147–170.
- LUO, GUOYU & SUN, MAO 2005 The effects of corrugation and wing planform on the aerodynamic force production of sweeping model insect wings. *Acta Mechanica Sinica* **21** (6), 531–541.

- MENG, XUEGUANG & SUN, MAO 2011 Aerodynamic effects of corrugation in flapping insect wings in forward flight. *Journal of Bionic Engineering* **8** (2), 140–150.
- MENG, XUE GUANG & SUN, MAO 2013 Aerodynamic effects of wing corrugation at gliding flight at low reynolds numbers. *Physics of Fluids* **25** (7), 071905.
- MILLER, LAURA A & PESKIN, CHARLES S 2004 When vortices stick: an aerodynamic transition in tiny insect flight. *Journal of Experimental Biology* **207** (17), 3073–3088.
- MUELLER, THOMAS J 1999 Aerodynamic measurements at low reynolds numbers for fixed wing micro-air vehicles. In *RTO AVT/VKI Special Course on Development and Operation of UAVs for Military and Civil Applications*.
- NARITA, YUMA & CHIBA, KAZUHISA 2024 Aerodynamics on a faithful hindwing model of a migratory dragonfly based on 3d scan data. *Journal of Fluids and Structures* **125**, 104080.
- NEWMAN, DJS & WOOTTON, RJ 1986 An approach to the mechanics of pleating in dragonfly wings. *Journal of Experimental Biology* **125** (1), 361–372.
- OBATA, AKIRA, SHINOHARA, SHOTAROU, AKIMOTO, KYOHEI, SUZUKI, KAKERU & SEKI, MIYUKI 2014 Aerodynamic bio-mimetics of gliding dragonflies for ultra-light flying robot. *Robotics* **3** (2), 163–180.
- OBATA, A & SINOHARA, S 2009 Flow visualization study of the aerodynamics of modeled dragonfly wings. *AIAA journal* **47** (12), 3043–3046.
- OKAMOTO, MASATO & EBINA, KEITA 2016 Effectiveness of large-camber circular arc airfoil at very low reynolds numbers. *Transactions of the Japan Society for Aeronautical and Space Sciences* **59** (5), 295–304.
- OTA, KEIGO, SUZUKI, KOSUKE & INAMURO, TAKAJI 2012 Lift generation by a two-dimensional symmetric flapping wing: immersed boundary-lattice boltzmann simulations. *Fluid Dynamics Research* **44** (4), 045504.
- PATERA, ANTHONY T 1984 A spectral element method for fluid dynamics: laminar flow in a channel expansion. *Journal of computational Physics* **54** (3), 468–488.
- RAJABI, HAMED, REZASEFAT, M, DARVIZEH, A, DIRKS, J-H, ESHGHI, SH, SHAFIEI, A, MOSTOFI, T MIRZABABAIE & GORB, STAS N 2016 A comparative study of the effects of constructional elements on the mechanical behaviour of dragonfly wings. *Applied Physics A* **122**, 1–13.
- REES, CHRISTOPHER JC 1975 Aerodynamic properties of an insect wing section and a smooth aerofoil compared. *Nature* **258** (5531), 141–142.
- RIVAL, DAVID E, KRIEGSEIS, JOCHEN, SCHAUB, PASCAL, WIDMANN, ALEXANDER & TROPEA, CAMERON 2014 Characteristic length scales for vortex detachment on plunging profiles with varying leading-edge geometry. *Experiments in fluids* **55** (1), 1–8.
- SANE, SANJAY P 2003 The aerodynamics of insect flight. *Journal of experimental biology* **206** (23), 4191–4208.
- SHYY, WEI, KANG, CHANG-KWON, CHIRARATTANANON, PAKPONG, RAVI, SRIDHAR & LIU, HAO 2016 Aerodynamics, sensing and control of insect-scale flapping-wing flight. *Proceedings of the Royal Society A: Mathematical, Physical and Engineering Sciences* **472** (2186), 20150712.
- SUDO, SEIICHI, TSUYUKI, KOJI & TANI, JUNJI 2000 Wing morphology of some insects. *JSME International Journal Series C Mechanical Systems, Machine Elements and Manufacturing* **43** (4), 895–900.
- TANG, JIAN, VIHERU, DRAGOS & SHYY, WEI 2008 Effects of reynolds number and flapping kinematics on hovering aerodynamics. *AIAA journal* **46** (4), 967–976.
- UHRHAN, MYRIAM JASMIN, BOMPHELY, RICHARD J & LIN, HUAI-TI 2024 Flow sensing on dragonfly wings. *Annals of the New York Academy of Sciences* .
- VARGAS, ABEL, MITTAL, RAJAT & DONG, HAIBO 2008 A computational study of the aerodynamic performance of a dragonfly wing section in gliding flight. *Bioinspiration & biomimetics* **3** (2), 026004.
- WANG, Z JANE 2000 Two dimensional mechanism for insect hovering. *Physical review letters* **85** (10), 2216.
- WANG, Z JANE & RUSSELL, DAVID 2007 Effect of forewing and hindwing interactions on aerodynamic forces and power in hovering dragonfly flight. *Physical review letters* **99** (14), 148101.
- ZHANG, JUN-DUO & HUANG, WEI-XI 2019 On the role of vortical structures in aerodynamic performance of a hovering mosquito. *Physics of Fluids* **31** (5).
- ZHANG, ZILONG, YIN, YAJUN, ZHONG, ZHENG & ZHAO, HONGXIAO 2015 Aerodynamic performance of dragonfly wing with well-designed corrugated section in gliding flight. *Computer Modeling in Engineering & Sciences* **109** (3), 285–302.